

High Order and High Resolution Nonlinear Weighted Compact Schemes

Akshay Subramaniam* and Man Long Wong*

Department of Aeronautics & Astronautics, Stanford University, Stanford, CA 94305, USA

Sanjiva K. Lele[†]

*Department of Aeronautics & Astronautics and Department of Mechanical Engineering,
Stanford University, Stanford, CA 94305, USA*

We present a new high-order Weighted Compact High Resolution (WCHR) scheme based on the Weighted Essentially Non-Oscillatory (WENO) and Weighted Compact Non-linear Schemes (WCNS) methods for shock and interface capturing in compressible flows that has greater resolution properties compared to traditional WENO schemes and WCNS. The main contribution is to use a compact (or spatially implicit) form for both the interpolation and derivative formulations. Since compact interpolation and derivative schemes tend to have much greater resolution properties compared to standard finite difference schemes, this new scheme has the ability to resolve more fine scale features while still providing sufficient dissipation to capture shocks and material interfaces robustly. Approximate dispersion relation characteristics of this scheme shows the superior resolution properties of the scheme compared to other WCNS's of similar order. Test cases for the Burgers and Euler equations demonstrate the ability of this scheme to capture discontinuities in a robust and stable manner while also localizing the required numerical dissipation to regions of discontinuities and hence preserving smooth flow features better in comparison to traditional WCNS and WENO schemes.

I. Introduction

Simulations of compressible flows that involve shock waves, material interfaces and turbulence have conflicting requirements. While capturing discontinuities like shock waves and material interfaces require added numerical dissipation, the fine scales of turbulence are severely affected by numerical dissipation. Hence, an adaptive method that switches between a low dissipation formulation near regions of smooth solutions to a formulation that adds sufficient dissipation at discontinuities is essential. In the past, WENO schemes¹⁻⁶ and WCNS⁷⁻¹¹ have been proposed as a method of providing this adaptation. These schemes capture shocks well and improvements like the WENO6-CU-M2⁶ and WCNS6-LD¹¹ schemes also add dissipation localized to regions of discontinuities. However, their resolution properties are limited by the underlying explicit finite difference and interpolation schemes. Lele¹² developed compact finite difference and interpolation schemes that are high order and have spectral-like resolution. These schemes cannot be used for problems with shocks unless some form of numerical regularization is used. Dissipation can be added explicitly¹³⁻¹⁵ to capture shocks and material interfaces with compact finite difference schemes using the LAD method proposed first by Cook.¹³ These schemes have good resolution properties, but tend to have oscillations near shocks and introduce additional time step limitations due to the explicitly added dissipation terms. In addition, filtering solutions at every time step for de-aliasing precludes these schemes from being Galilean invariant. Deng et al.⁷ used a compact finite difference scheme in the context of WCNS but still used an explicit interpolation scheme that limits the effective resolution of the overall scheme. Ghosh et al.¹⁶ developed an upwind-biased compact reconstruction WENO scheme called CRWENO. However, the upwind-biased scheme is excessively

*Graduate Research Assistant, Department of Aeronautics & Astronautics, Stanford University, and AIAA Student Member

[†]Professor, Department of Aeronautics & Astronautics and Department of Mechanical Engineering, Stanford University, and AIAA Associate Fellow

dissipative in regions of smooth flow and hence damps the fine scales of turbulence. In this paper, we develop a new scheme based on the WCNS formalism that uses a compact form for both the underlying finite difference scheme and the interpolation scheme that provides higher resolution and more localized dissipation compared to traditional WCNS and WENO schemes.

II. Numerical method

For simplicity and ease of comprehension, a scalar conservation law of the following form is considered in this section

$$\frac{\partial u}{\partial t} + \frac{\partial \mathcal{F}(u)}{\partial x} = 0 \quad (1)$$

where u is the conserved scalar quantity and $\mathcal{F}(u)$ is the flux as a function of u . The equation above is discretized on a uniform grid with N cell nodes and the solution u on the cell node at position x_j is denoted by $u_j \forall j \in \{0, 1, \dots, N-1\}$. The cell midpoints are indexed by half integer values $\{-\frac{1}{2}, \frac{1}{2}, 1 + \frac{1}{2}, \dots, N - \frac{1}{2}\}$. Figure 1 shows a schematic with the cell nodes and midpoints detailed.

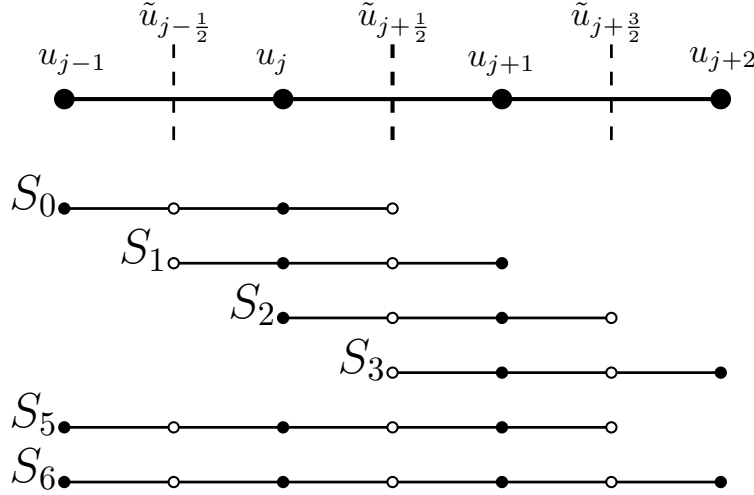


Figure 1. Stencil for the WCHR6 scheme

II.A. Compact finite difference

The flux derivative in Equation 1 is written in terms of the nodal values of the flux at the cell nodes $f = \mathcal{F}(u)$ computed from the solution u at the cell nodes and using the fluxes at the edges \tilde{f} like in Liu et al.¹⁷ The 6th order compact finite difference stencil used in this work is given by:¹⁷

$$\alpha f'_{j-1} + f'_j + \alpha f'_{j+1} = a \frac{\tilde{f}_{j+\frac{1}{2}} - \tilde{f}_{j-\frac{1}{2}}}{h} + b \frac{f_{j+1} - f_{j-1}}{2h} \quad (2)$$

where $\alpha = -\frac{1}{12}$, $a = \frac{16}{9}$ and $b = -\frac{17}{18}$.

II.B. Weighted compact interpolation

To get the midpoint fluxes \tilde{f} , we first need to get the interpolated midpoint values of the conserved scalar \tilde{u} and compute the midpoint fluxes as $\tilde{f} = \mathcal{F}(\tilde{u})$. The novel aspect of this work is to use a compact interpolation scheme that provides higher resolution quality to the solutions compared to explicit Lagrangian interpolations and can hence be useful for simulations where a large range of scales are present. In this section, we present the scheme used to get the left biased interpolated values. To get the right biased interpolated values at edge $j + 1/2$, all the sub-stencils can be flipped with respect to the $j + 1/2$ edge. Figure 1 shows the stencils for four 3rd order interpolation schemes S_0 , S_1 , S_2 and S_3 respectively used to build a 5th order upwind-biased interpolation scheme S_5 and a 6th order central interpolation scheme S_6 . The four 3rd order interpolation

schemes are given by:

$$S_0 : \quad \frac{3}{4}\tilde{u}_{j-\frac{1}{2}} + \frac{1}{4}\tilde{u}_{j+\frac{1}{2}} = \frac{1}{4}u_{j-1} + \frac{3}{4}u_j \quad (3)$$

$$S_1 : \quad \frac{1}{4}\tilde{u}_{j-\frac{1}{2}} + \frac{3}{4}\tilde{u}_{j+\frac{1}{2}} = \frac{3}{4}u_j + \frac{1}{4}u_{j+1} \quad (4)$$

$$S_2 : \quad \frac{3}{4}\tilde{u}_{j+\frac{1}{2}} + \frac{1}{4}\tilde{u}_{j+\frac{3}{2}} = \frac{1}{4}u_j + \frac{3}{4}u_{j+1} \quad (5)$$

$$S_3 : \quad \frac{1}{4}\tilde{u}_{j+\frac{1}{2}} + \frac{3}{4}\tilde{u}_{j+\frac{3}{2}} = \frac{3}{4}u_{j+1} + \frac{1}{4}u_{j+2} \quad (6)$$

The 5th order linear upwind-biased and 6th order linear central interpolation schemes can be obtained by linear combinations of the four 3rd order stencils:

$$S_5 := \sum_{k=0}^3 d_k^{\text{upwind}} S_k \quad (7)$$

$$S_6 := \sum_{k=0}^3 d_k^{\text{central}} S_k \quad (8)$$

where $d^{\text{upwind}} = [\frac{1}{4}, \frac{1}{2}, \frac{1}{4}, 0]$ are the linear weights for the upwind-biased interpolation and $d^{\text{central}} = [\frac{1}{8}, \frac{3}{8}, \frac{3}{8}, \frac{1}{8}]$ are the linear weights for the central interpolation. The expanded forms of the two interpolation methods are given below by

$$S_5 : \quad \frac{5}{16}\tilde{u}_{j-\frac{1}{2}} + \frac{5}{8}\tilde{u}_{j+\frac{1}{2}} + \frac{1}{16}\tilde{u}_{j+\frac{3}{2}} = \frac{1}{16}u_{j-1} + \frac{5}{8}u_j + \frac{5}{16}u_{j+1} \quad (9)$$

$$S_6 : \quad \frac{3}{16}\tilde{u}_{j-\frac{1}{2}} + \frac{5}{8}\tilde{u}_{j+\frac{1}{2}} + \frac{3}{16}\tilde{u}_{j+\frac{3}{2}} = \frac{1}{32}u_{j-1} + \frac{15}{32}u_j + \frac{15}{32}u_{j+1} + \frac{1}{32}u_{j+2} \quad (10)$$

II.C. Weighted Compact High Resolution (WCHR) scheme

While midpoint values \tilde{u} can be obtained by either one of the linear compact interpolations in Equation 9 and 10 for smooth solutions, neither one provides sufficient numerical dissipation to avoid unphysical oscillations in interpolated values around discontinuities. The aforementioned compact (or implicit) interpolation using the nonlinear weighting technique from WENO/WCNS method is proposed to give sufficient numerical dissipation at discontinuities while also having high resolution and minimizing dissipation for features in smooth regions. The nonlinear compact interpolation scheme $S_{\text{nonlinear}}$ at a midpoint $x_{j+\frac{1}{2}}$ is obtained using a combination of the four 3rd order compact schemes $S_0 - S_3$ as

$$S_{\text{nonlinear}} := \sum_{k=0}^3 \omega_k S_k \quad (11)$$

where ω_k is the nonlinear weight for the 3rd order interpolation scheme S_k . In regions where the solution is smooth, $\omega_k \rightarrow d_k^{\text{central}}$ so that a central interpolation scheme is used and no additional numerical dissipation is introduced.

The localized dissipation (LD) nonlinear weights in modified form of Wong and Lele¹¹ is given by

$$\omega_k = \begin{cases} (1 - \sigma)\omega_k^{\text{upwind}} + \sigma\omega_k^{\text{central}}, & \text{if } R(\tau) > \alpha_{RL}^{\tau}, \forall k = 0, 1, 2, 3 \\ \omega_k^{\text{central}}, & \text{otherwise} \end{cases} \quad (12)$$

where ω_k^{upwind} and $\omega_k^{\text{central}}$ are nonlinear weights for the upwind biased and central schemes respectively and are given by:

$$\omega_k^{\text{upwind}} = \frac{\alpha_k}{\sum_{k=0}^3 \alpha_k}, \quad \alpha_k^{\text{upwind}} = d_k^{\text{upwind}} \left(1 + \left(\frac{\tau_5}{\beta_k + \epsilon} \right)^p \right), \quad k = 0, 1, 2, 3 \quad (13)$$

$$\omega_k^{\text{central}} = \frac{\alpha_k}{\sum_{k=0}^3 \alpha_k}, \alpha_k^{\text{central}} = d_k^{\text{central}} \left(C + \left(\frac{\tau_6}{\beta_k + \epsilon} \right)^q \right), k = 0, 1, 2, 3 \quad (14)$$

ω_3^{upwind} is always zero since d_3^{upwind} is zero. $\epsilon = 10^{-6}$ is a small constant to prevent division by zero. p and q are integers and C is a constant determining the scale-separation capability of the scheme. τ_5 and τ_6 are fifth order and sixth order reference smoothness indicators respectively:

$$\tau_5 = |\beta_2 - \beta_0| \quad (15)$$

$$\tau_6 = |\beta_3 - \beta_{\text{avg}}| \quad (16)$$

where

$$\beta_{\text{avg}} = \frac{1}{8} (\beta_0 + 6\beta_1 + \beta_2) \quad (17)$$

β_k are smoothness indicators defined by Liu et al.¹⁰ $R(\tau)$ is a sensor to distinguish smooth and non-smooth regions and is defined as

$$R(\tau) = \frac{\tau_6}{\beta_{\text{avg}} + \epsilon} \quad (18)$$

α_{RL}^τ is a constant determining the cut-off for the hybridization. $0 \leq \sigma \leq 1$ is a blending function blending the upwind-biased and central interpolations. σ should be close to one in regions near high wavenumber features. In this paper, the following sensor is used to provide the value of σ :

$$\sigma_{j+\frac{1}{2}} = \theta_{j+\frac{1}{2}} \quad (19)$$

where $\theta_{j+\frac{1}{2}} = \max(\theta_j, \theta_{j+1})$. θ_j is defined as

$$\theta_j = \frac{|\alpha_{j+\frac{1}{2}} - \alpha_{j-\frac{1}{2}}|}{\alpha_{j+\frac{1}{2}} + \alpha_{j-\frac{1}{2}} + \epsilon} \quad (20)$$

$$\alpha_{j+\frac{1}{2}} = |u_{j+1} - u_j| \quad (21)$$

The parameters for computing the non-linear weights in the WCHR6 scheme (the 6 at the end indicates the 6th order accuracy of the scheme) are given in Table 1. For a discussion on choice of these parameters, see Wong and Lele,¹¹ and Hu et. al.⁶ The parameters used here provide stable results while preserving the high resolution property of the underlying compact interpolation scheme. They are also chosen so that added numerical dissipation is localized to regions of discontinuity and have minimal effect on regions where the solution is smooth.

For the scalar conservation equation (Equation 1), the algorithm for one time integration sub-step is given below:

1. Compute the left biased and right biased interpolated solution values \tilde{u}_L and \tilde{u}_R using the weighted nonlinear compact interpolation described above.
2. Compute the flux at the cell nodes $f = \mathcal{F}(u)$.
3. Compute the flux at the cell edges using a flux-splitting method $\tilde{f} = \mathcal{F}^{\text{split}}(\tilde{u}_L, \tilde{u}_R)$
4. Using the fluxes f and \tilde{f} , compute the flux derivative using Equation 2
5. Update the solution based on the flux derivative computed.

Table 1. Parameters for computing the non-linear weights in the WCHR6 scheme.

Parameter	Value
C	2×10^3
p	2
q	2
α_{RL}^τ	40

II.C.1. Approximate dispersion relation

For linear schemes, the dissipation and dispersion characteristics can be characterized using a dispersion relation analysis like in Lele.¹² This is not possible for non-linear schemes, but Pirozzoli¹⁸ developed an Approximate Dispersion Relation (ADR) technique to characterize the dispersion and dissipation characteristics of general schemes. Results from ADR analysis are shown in Figure 2 for the WCHR6 scheme and three WCNS schemes using explicit derivative and interpolation schemes with the traditional JS nonlinear weights,¹ the Z nonlinear weights⁴ and the LD nonlinear weights.¹¹ Figure 2(a) shows the real part of the dispersion relation. Here, we see that the WCHR6 scheme outperforms the other schemes in dispersion error. Figure 2(c) shows the dispersion error for the four schemes on a semi-log plot. Given a threshold ϵ_{res} for the maximum tolerable dispersion error, a resolving efficiency of the different schemes can be computed. The resolving efficiency is defined as the fraction of Nyquist wavenumber that the scheme can resolve within the given dispersion error tolerance ϵ_{res} . In Figure 2(c), the black dashed line represents $\epsilon_{\text{res}} = 0.01$ and the colored dashed lines represent the maximum wavenumber that each scheme can resolve given this threshold. Table 2 shows the resolving efficiency for the four different schemes. From this, we see that the WCHR6 scheme has much higher resolution ability compared to other schemes of similar order of accuracy ($\sim 53\%$ more than the WCNS5-JS scheme). Figure 2(b) shows the dissipation characteristic of the four schemes. From this, we see that the WCNS5-JS and WCNS5-Z schemes have dissipation even at low wavenumbers but the WCHR6 and the WCNS6-LD schemes have localized dissipation only at high wavenumbers. The high resolution and localized dissipation characteristics of the WCHR6 scheme are especially important for problems involving turbulence where low resolution and excessive dissipation can curtail the range of scales in the problem.

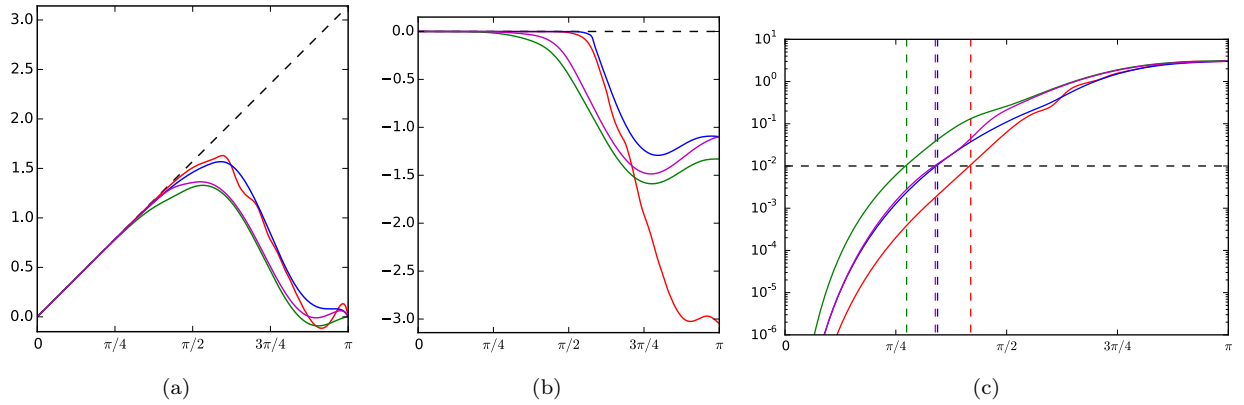


Figure 2. ADR results for four schemes: WCNS5-JS (green), WCNS5-Z (magenta), WCNS6-LD (blue) and WCHR6 (red). (a) Real part of the dispersion relation (b) Imaginary part of the dispersion error characterizing the added dissipation and (c) Solid lines are the dispersion error (deviation of plot (a) from ideal) for the different schemes. The black dashed line is an error threshold level of 10^{-2} and the colored dashed lines indicate the reduced wavenumber beyond which the dispersion error exceeds the threshold.

Table 2. Resolving efficiency of different schemes for $\epsilon_{\text{res}} = 0.01$.

Scheme	Resolving efficiency	Improvement over WCNS5-JS
WCNS5-JS	0.274	0%
WCNS5-Z	0.339	23.7%
WCNS6-LD	0.344	25.5%
WCHR6	0.419	52.9%

II.D. Extension to Euler equations

The inviscid 1D-1C Euler equations are given by

$$\frac{\partial \mathbf{Q}}{\partial t} + \frac{\partial \mathbf{F}(\mathbf{Q})}{\partial x} = 0 \quad (22)$$

where

$$\mathbf{Q} = \begin{pmatrix} \rho \\ \rho u \\ E \end{pmatrix} \quad \text{and} \quad \mathbf{F}(\mathbf{Q}) = \begin{pmatrix} \rho u \\ \rho u^2 + p \\ (E + p)u \end{pmatrix} \quad (23)$$

where ρ is the density, u is the x velocity, E is the total energy and $p = (\gamma - 1)(E - \frac{1}{2}\rho u^2)$ is the pressure.

The WCHR6 scheme can be applied to the Euler equations in a similar fashion to the scalar conservation law. Equation 2 can be used to get the flux derivative based on the flux at the nodes $\mathbf{F} = \mathbf{F}(\mathbf{Q})$ and the flux at the midpoints $\tilde{\mathbf{F}} = \mathbf{F}^{\text{Riemann}}(\tilde{\mathbf{Q}}_L, \tilde{\mathbf{Q}}_R)$ where $\tilde{\mathbf{Q}}_L$ and $\tilde{\mathbf{Q}}_R$ are the left and right interpolated solution vectors at the midpoints and $\mathbf{F}^{\text{Riemann}}$ is the flux from a Riemann solver (see Section II.D.2 for details on the Riemann solver used here). The interpolated solution vector at the edges can be computed by directly interpolating the conserved variables or interpolating the primitive variables (ρ, u, p) using the weighted compact interpolation. Although these methods work and provide stable results they are excessively dissipative. A more natural way to perform the interpolation is to interpolate the characteristic variables since the equations are decoupled in the characteristic space. Interpolating the characteristic variables provides much more localized dissipation and hence can preserve smooth flow features better. The characteristic decomposition and interpolation with the WCHR6 scheme is described in the section below.

II.D.1. Characteristic decomposition

For a 1D-1C Euler equation system, the three characteristic variables at edge ξ^0 , ξ^1 and ξ^2 are given by

$$\begin{pmatrix} \xi^0 \\ \xi^1 \\ \xi^2 \end{pmatrix} = \mathbf{A}^{RL} \cdot \begin{pmatrix} \rho \\ u \\ p \end{pmatrix} \quad (24)$$

where \mathbf{A}^{RL} is the matrix of the left eigenvectors of the linearized Euler system given by

$$\mathbf{A}^{RL} = \begin{pmatrix} 0 & -\frac{\rho c_s}{2} & \frac{1}{2} \\ 1 & 0 & -\frac{1}{c_s^2} \\ 0 & \frac{\rho c_s}{2} & \frac{1}{2} \end{pmatrix} \quad (25)$$

where $c_s = \sqrt{\gamma p / \rho}$ is the speed of sound in the medium.

At a midpoint $j + 1/2$, the characteristic variables for the whole stencil are computed using the same left eigenvector matrix $\mathbf{A}_{j+1/2}^{RL}$ given by the Roe average of the matrix at node j and $j + 1$ to maintain consistency between the transforms to and back from the characteristic space.

$$\alpha_{j+\frac{1}{2}} \tilde{\xi}_{j-\frac{1}{2}}^k + \beta_{j+\frac{1}{2}} \tilde{\xi}_{j+\frac{1}{2}}^k + \gamma_{j+\frac{1}{2}} \tilde{\xi}_{j+\frac{3}{2}}^k = a_{j+\frac{1}{2}} \xi_{j-1}^k + b_{j+\frac{1}{2}} \xi_j^k + c_{j+\frac{1}{2}} \xi_{j+1}^k + d_{j+\frac{1}{2}} \xi_{j+2}^k \quad \forall k \in \{0, 1, 2\} \quad (26)$$

where $\alpha_{j+\frac{1}{2}}$, $\beta_{j+\frac{1}{2}}$, $\gamma_{j+\frac{1}{2}}$, $a_{j+\frac{1}{2}}$, $b_{j+\frac{1}{2}}$, $c_{j+\frac{1}{2}}$ and $d_{j+\frac{1}{2}}$ are the coefficients obtained from the weighted nonlinear interpolation method described in Section II.C. Written in terms of the primitive variables at the cell nodes $\mathbf{V} = (\rho, u, p)^T$ and the midpoint interpolated primitive variables $\tilde{\mathbf{V}} = (\tilde{\rho}, \tilde{u}, \tilde{p})^T$, the above equation becomes

$$\alpha_{j+\frac{1}{2}} \mathbf{A}_{j+\frac{1}{2}}^{RL} \cdot \tilde{\mathbf{V}}_{j-\frac{1}{2}} + \beta_{j+\frac{1}{2}} \mathbf{A}_{j+\frac{1}{2}}^{RL} \cdot \tilde{\mathbf{V}}_{j+\frac{1}{2}} + \gamma_{j+\frac{1}{2}} \mathbf{A}_{j+\frac{1}{2}}^{RL} \cdot \tilde{\mathbf{V}}_{j+\frac{3}{2}} = a_{j+\frac{1}{2}} \mathbf{A}_{j+\frac{1}{2}}^{RL} \cdot \mathbf{V}_{j-1} + b_{j+\frac{1}{2}} \mathbf{A}_{j+\frac{1}{2}}^{RL} \cdot \mathbf{V}_j + c_{j+\frac{1}{2}} \mathbf{A}_{j+\frac{1}{2}}^{RL} \cdot \mathbf{V}_{j+1} + d_{j+\frac{1}{2}} \mathbf{A}_{j+\frac{1}{2}}^{RL} \cdot \mathbf{V}_{j+2} \quad (27)$$

Hence, with the characteristic decomposition, the interpolation reduces to one block tri-diagonal system of equations instead of three tri-diagonal systems of equations if just the primitive variables are interpolated.

Figure 3 shows the matrix structure for the left biased characteristic based weighted compact interpolation for the initial conditions of the Shu-Osher problem (Equation 36) with 80 points in the domain. Since the matrix is a block tri-diagonal system, the size of the matrix is 240×240 and the full matrix structure is shown in Figure 3(a). Figure 3(b) shows the first 50×50 portion of the interpolation matrix. Here, we see that across the shock at index ~ 25 , the matrix decouples. This means that the interpolation stencil never crosses the shock. Figure II.B shows the left and right interpolated density, velocity and pressure. Since the interpolation stencil never crosses the shock, the interpolation is virtually perfect and no spurious oscillations are observed.

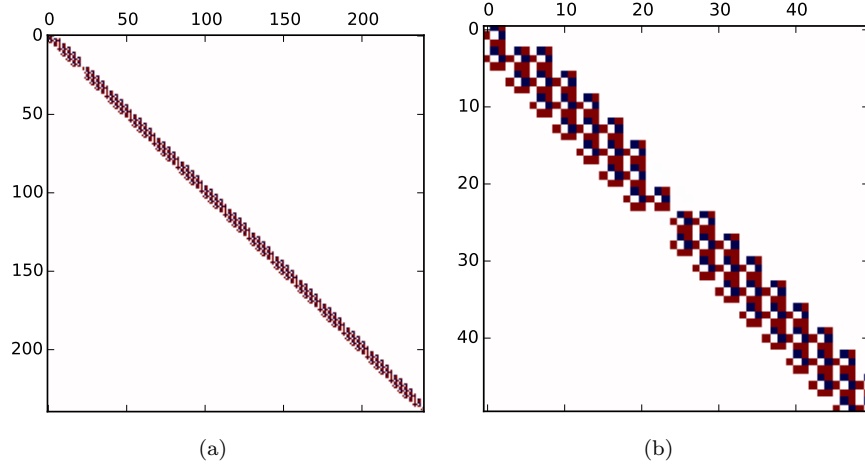


Figure 3. (a) The full block tri-diagonal matrix structure for the characteristic decomposition for initial condition of the Shu-Osher problem with 80 points. (b) The top 50×50 portion of the matrix shows that the interpolation is decoupled across the shock.

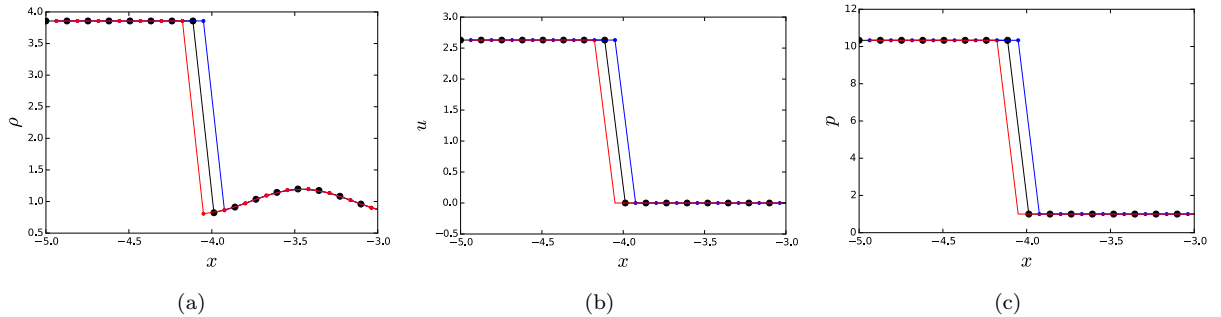


Figure 4. (a) Density, (b) velocity and (c) pressure plots of the prescribed nodal values (black), left interpolated edge values (blue) and right interpolated face values (red) for initial condition of the Shu-Osher problem with 80 points.

II.D.2. Riemann solver

The flux from HLLC Riemann solver \mathbf{F}^{HLLC} is used as the midpoint flux $\tilde{\mathbf{F}}$.

$$\mathbf{F}^{\text{HLLC}} = \frac{1 + \text{sign}(s_*)}{2} \left[\mathbf{F}(\tilde{\mathbf{Q}}_L) + s_- (\mathbf{Q}_{*L} - \tilde{\mathbf{Q}}_L) \right] + \frac{1 - \text{sign}(s_*)}{2} \left[\mathbf{F}(\tilde{\mathbf{Q}}_R) + s_+ (\mathbf{Q}_{*R} - \tilde{\mathbf{Q}}_R) \right] \quad (28)$$

where L, R are the left and right states respectively. With $K = L$ or R , the star state for single-species flow is defined as

$$\mathbf{Q}_{*K} = \chi_{*K} \begin{bmatrix} \rho_K \\ \rho_K s_* \\ E_K + (s_* - u_K) \left(\rho_K s_* + \frac{p_K}{s_K - u_K} \right) \end{bmatrix} \quad (29)$$

where

$$\chi_{*K} = \frac{s_K - u_K}{s_K - s_*} \quad (30)$$

We use the waves speeds suggested by Einfeldt et al.:¹⁹

$$s_- = \min(0, s_L), \quad s_+ = \max(0, s_R) \quad (31)$$

and

$$s_L = \min(\bar{u} - \bar{c}, u_L - c_L), \quad s_R = \max(\bar{u} + \bar{c}, u_R + c_R) \quad (32)$$

where \bar{u} and \bar{c} are the averages from the left and right states. Roe averages are used in this paper. Following Batten et al.,²⁰ the wave speed for the star state is:

$$s_* = \frac{p_R - p_L + \rho_L u_L (s_L - u_L) - \rho_R u_R (s_R - u_R)}{\rho_L (s_L - u_L) - \rho_R (s_R - u_R)} \quad (33)$$

III. Results

In this section, we present results using the WCHR6 scheme for the Burgers equation and Euler equations. All results here use the 5 stage 4th order Runge-Kutta scheme.²¹

III.A. Burgers equation

The Burgers equation is given by Equation 1 with $\mathcal{F}(u) = \frac{1}{2}u^2$. The initial conditions are given by

$$u(x, t = 0) = \frac{1}{4\pi} \sin(2\pi x) \quad (34)$$

on a domain $x \in [0, 1]$. This initial condition causes the initially sinusoidal wave to steepen and eventually form a shock at $x = 0.5$. The ability of the WCHR6 scheme to capture discontinuities is tested here in a scalar conservation law.

Figure 5 shows the solution at $t = 3$ using 40 grid points and a CFL of 0.7 in comparison to a reference solution computed using 2000 points. We see that the shock is captured very sharply with negligible effect on the smooth parts of the solution.

III.B. Sod shock tube problem

This is a one-dimensional shock tube problem introduced by Sod.²² The problem consists of the propagation of a shock wave, a contact discontinuity and an expansion fan. The initial conditions are

$$(\rho, u, p) = \begin{cases} (1, 0, 1), & x < 0 \\ (0.125, 0, 0.1), & x \geq 0 \end{cases} \quad (35)$$

The ratio of specific heats γ is 1.4. The computational domain has size $x \in [-0.5, 0.5]$. Simulations are performed with constant time steps $\Delta t = 0.002$ on a uniform grid composed of 100 grid points where $\Delta x = 0.01$.

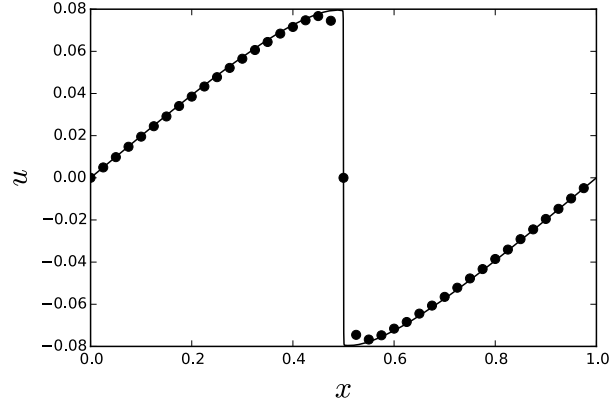


Figure 5. Solution for Burgers equation using the WCHR6 scheme with 40 points (black circles) and the reference solution computed with 2000 points (solid black line) at $t = 3$. A CFL number of 0.7 was used for both the cases.

Comparison between the exact solution and the numerical solution for the density, velocity and pressure at $t = 0.2$ is shown in Figures 6(a)-6(c). Figures 6(d)-6(f) compare the density profile obtained using the WCHR6 scheme and the WCNS6-LD scheme. Both the WCHR6 and WCNS6-LD scheme capture the shock and contact discontinuity well. At the expansion fan though, the WCNS6-LD scheme has a significant undershoot that the WCHR6 scheme does not have.

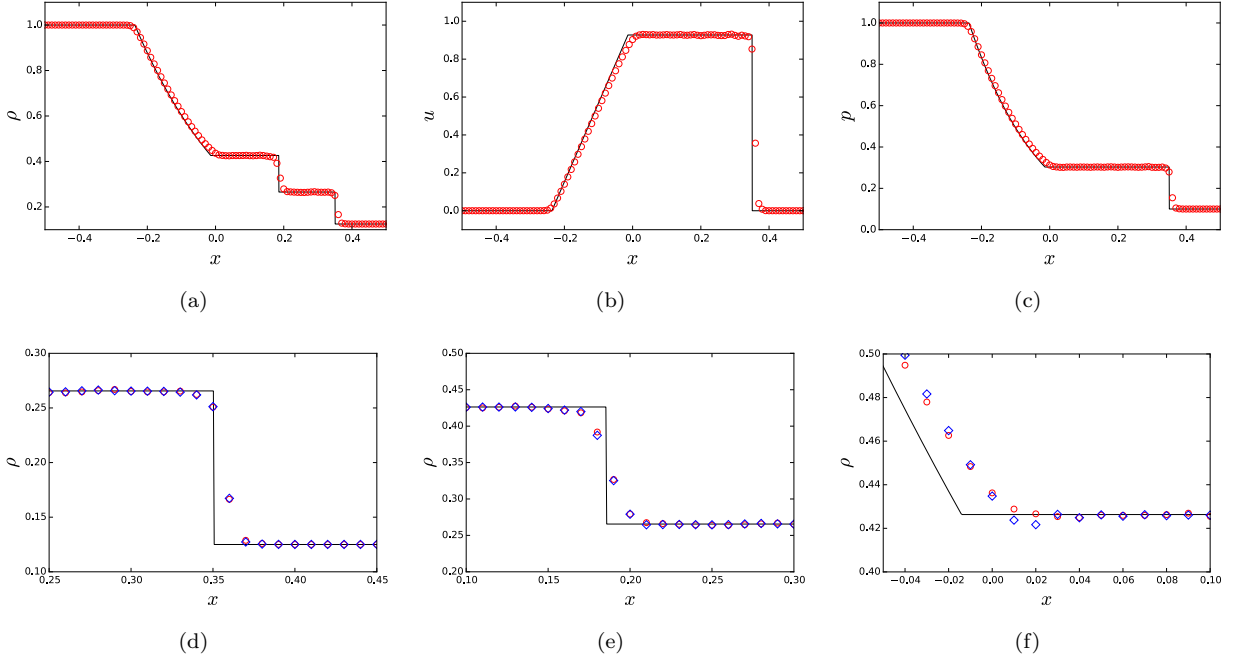


Figure 6. (a) Density plot, (b) velocity plot, (c) pressure plot, (d) zoomed-in density plot near shock, (e) zoomed-in density plot near contact discontinuity, and (f) zoomed-in density plot near expansion fan. Blue diamonds: explicit WCNS6-LD; red circles: WCHR6; black solid line: exact solution

III.C. Shu-Osher problem

This one-dimensional problem first proposed by Shu and Osher²³ involves the interaction of a Mach 3 shock wave with an entropy wave. This interaction creates a high wavenumber entropy wave and a non-linear acoustic wave that steepens and forms a shock train. This problem can hence assess the ability of a scheme to both capture discontinuities well, while also retaining the smooth features of the solution. The initial

conditions are given by

$$(\rho, u, p) = \begin{cases} (3.857143, 2.62936, 10.33339), & x < -4 \\ (1 + 0.2 \sin(5x), 0, 1), & x \geq -4 \end{cases} \quad (36)$$

The ratio of specific heats γ is 1.4. The spatial domain of the problem is $x \in [-5, 5]$. Simulations are conducted with constant time steps $\Delta t = 0.002$ on a uniform grid with 200 grid points where $\Delta x = 0.05$. A reference solution is computed using the WCNS6-LD scheme with 2000 points and time step of $\Delta t = 0.0002$. All results shown here are at time $t = 1.8$.

Figure 7(a) shows the density profile at $t = 1.8$ obtained using the WCHR6 scheme compared to the reference solution. The WCHR6 scheme captures the Mach 3 shock well and also captures the high wavenumber entropy wave just upstream of the shock without too much dissipation. Figure 7(b) compares the solutions obtained using the WCHR6 scheme and the CRWENO5-LD scheme. Both these schemes use a compact formulation for the interpolation (reconstruction in the CRWENO case) and capture the shock at $x \approx -0.5$ equally well with no spurious oscillations. However, the CRWENO5-LD scheme dissipates the high wavenumber entropy wave significantly which is not seen in the results from the WCHR6 scheme. Figures 7(c) and 7(d) compare the WCHR6 and WCNS6-LD schemes. Both the WCHR6 and WCNS6-LD schemes give good results in the post shock entropy wave region. The WCNS6-LD scheme has significant undershoot at the shocks while the WCHR6 scheme captures the shock well with no significant undershoot or oscillations.

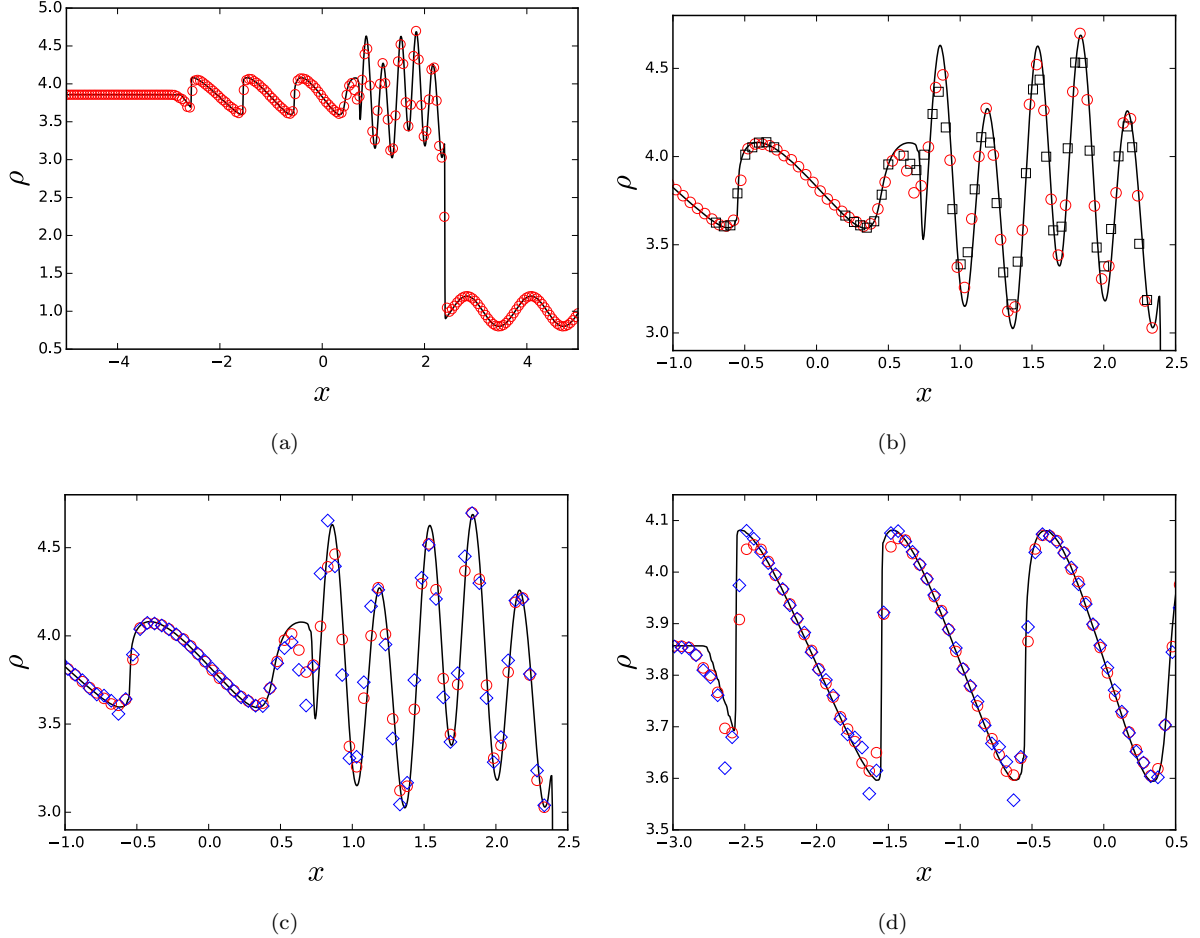


Figure 7. (a) Density plot, (b-d) zoomed-in density plots. Blue diamonds: explicit WCNS6-LD; red circles: WCHR6; black squares: CRWENO5-LD, black solid line: exact solution

IV. Summary and future work

In summary, we developed a new Weighted Compact High Resolution (WCHR) scheme that has higher resolution and more localized dissipation compared to other WCNS/WENO schemes. The scheme was presented for use with scalar conservation equations and then extended to the Euler equations in one dimension. The block tri-diagonal characteristic decomposition method was shown to be effective at interpolating the primitive variables across shocks. Approximate Dispersion Relation (ADR) analysis of the scheme showed the superior resolution ability of the scheme compared to other WCNS's of similar order of accuracy. Results for the inviscid Burgers equation and the Sod shock tube problem showed the ability of the scheme to capture shocks well. Results from the Shu-Osher problem showed the ability of the scheme to capture shocks well with sufficient numerical dissipation while minimizing the effect on smooth regions of the flow.

For the final manuscript, we plan on performing additional tests like the 1D Noh problem and the 2D problem of shock interaction with a combined vorticity and entropy wave. In addition to these test problems, the WCHR6 scheme will be extended to higher orders (8th and 10th orders) to further improve their resolution and dissipation characteristics.

References

- ¹Jiang, G.-S. and Shu, C.-W., "Efficient implementation of weighted ENO schemes." Tech. rep., DTIC Document, 1995.
- ²Henrick, A. K., Aslam, T. D., and Powers, J. M., "Mapped weighted essentially non-oscillatory schemes: achieving optimal order near critical points," *Journal of Computational Physics*, Vol. 207, No. 2, 2005, pp. 542–567.
- ³Martín, M. P., Taylor, E. M., Wu, M., and Weirs, V. G., "A bandwidth-optimized WENO scheme for the effective direct numerical simulation of compressible turbulence," *Journal of Computational Physics*, Vol. 220, No. 1, 2006, pp. 270–289.
- ⁴Borges, R., Carmona, M., Costa, B., and Don, W. S., "An improved weighted essentially non-oscillatory scheme for hyperbolic conservation laws," *Journal of Computational Physics*, Vol. 227, No. 6, 2008, pp. 3191–3211.
- ⁵Hu, X., Wang, Q., and Adams, N., "An adaptive central-upwind weighted essentially non-oscillatory scheme," *Journal of Computational Physics*, Vol. 229, No. 23, 2010, pp. 8952–8965.
- ⁶Hu, X. and Adams, N., "Scale separation for implicit large eddy simulation," *Journal of Computational Physics*, Vol. 230, No. 19, 2011, pp. 7240–7249.
- ⁷Deng, X. and Zhang, H., "Developing high-order weighted compact nonlinear schemes," *Journal of Computational Physics*, Vol. 165, No. 1, 2000, pp. 22–44.
- ⁸Nonomura, T., Iizuka, N., and Fujii, K., "Increasing order of accuracy of weighted compact nonlinear scheme," *AIAA Paper*, Vol. 893, 2007.
- ⁹Zhang, S., Jiang, S., and Shu, C.-W., "Development of nonlinear weighted compact schemes with increasingly higher order accuracy," *Journal of Computational Physics*, Vol. 227, No. 15, 2008, pp. 7294–7321.
- ¹⁰Liu, X., Zhang, S., Zhang, H., and Shu, C.-W., "A new class of central compact schemes with spectral-like resolution II: Hybrid weighted nonlinear schemes," *Journal of Computational Physics*, Vol. 284, 2015, pp. 133–154.
- ¹¹Wong, M. L. and Lele, S. K., "Improved Weighted Compact Nonlinear Scheme for Flows with Shocks and Material Interfaces: Algorithm and Assessment," *AIAA Paper 2016-1807*, 2016.
- ¹²Lele, S. K., "Compact finite difference schemes with spectral-like resolution," *Journal of Computational Physics*, Vol. 103, No. 1, 1992, pp. 16–42.
- ¹³Cook, A. W., "Artificial fluid properties for large-eddy simulation of compressible turbulent mixing," *Physics of Fluids (1994-present)*, Vol. 19, No. 5, 2007, pp. 055103.
- ¹⁴Fiorina, B. and Lele, S. K., "An artificial nonlinear diffusivity method for supersonic reacting flows with shocks," *Journal of Computational Physics*, Vol. 222, No. 1, 2007, pp. 246–264.
- ¹⁵Kawai, S. and Lele, S. K., "Localized artificial diffusivity scheme for discontinuity capturing on curvilinear meshes," *Journal of Computational Physics*, Vol. 227, No. 22, 2008, pp. 9498–9526.
- ¹⁶Ghosh, D. and Baeder, J. D., "Compact reconstruction schemes with weighted ENO limiting for hyperbolic conservation laws," *SIAM Journal on Scientific Computing*, Vol. 34, No. 3, 2012, pp. A1678–A1706.
- ¹⁷Liu, X., Zhang, S., Zhang, H., and Shu, C.-W., "A new class of central compact schemes with spectral-like resolution I: Linear schemes," *Journal of Computational Physics*, Vol. 248, 2013, pp. 235–256.
- ¹⁸Pirozzoli, S., "On the spectral properties of shock-capturing schemes," *Journal of Computational Physics*, Vol. 219, No. 2, 2006, pp. 489–497.
- ¹⁹Einfeldt, B., Munz, C.-D., Roe, P. L., and Sjögren, B., "On Godunov-type methods near low densities," *Journal of Computational Physics*, Vol. 92, No. 2, 1991, pp. 273–295.
- ²⁰Batten, P., Clarke, N., Lambert, C., and Causon, D., "On the choice of wavespeeds for the HLLC Riemann solver," *SIAM Journal on Scientific Computing*, Vol. 18, No. 6, 1997, pp. 1553–1570.
- ²¹Kennedy, C. A., Carpenter, M. H., and Lewis, R. M., "Low-storage, explicit Runge–Kutta schemes for the compressible Navier–Stokes equations," *Applied numerical mathematics*, Vol. 35, No. 3, 2000, pp. 177–219.
- ²²Sod, G. A., "A survey of several finite difference methods for systems of nonlinear hyperbolic conservation laws," *Journal of Computational Physics*, Vol. 27, No. 1, 1978, pp. 1–31.
- ²³Shu, C.-W. and Osher, S., "Efficient implementation of essentially non-oscillatory shock-capturing schemes," *Journal of Computational Physics*, Vol. 77, No. 2, 1988, pp. 439–471.